Laser and Particle Beams (2017), *35*, 597–609.

doi:10.1017/S0263034617000611

Laser-generated Richtmyer–Meshkov and Rayleigh–Taylor instabilities. III. Near-peripheral region of Gaussian spot

STJEPAN LUGOMER*

Rudjer Boskovic Institute, Center of Excellence for Advanced Materials and Sensing Devices, Bijenicka c. 54, 10000 Zagreb, Croatia

(Received 28 June 2017; Accepted 17 August 2017)

Abstract

Dynamics and organization of laser-generated three-dimensional (3D) Richtmyer–Meshkov (RMI) and Rayleigh–Taylor instabilities (RMI and RTI) on metal target in the semiconfined configuration are different in the central region (CR) (Lugomer, 2016), near central region (NCR) (Lugomer, 2017) and the near periphery region (NPR) of the Gaussian-like spot. The RMI/RTI in the NPR evolve from the shock and series of reshocks associated with lateral expansion and increase of the vapor density, decrease of the Atwood number and momentum transfer. Scanning electron micrographs show irregular (chaotic) web of the base-plane walls, and mushroom spikes on its nodal points with disturbed two-dimensional (2D) lattice organization. Lattice disturbance is caused by the incoherent wavy motion of background fluid due to fast reshocks, which after series of reflections change their strength and direction. Reconstruction of the disturbed lattice reveals rectangular lattice of mushroom spikes with p_2mm symmetry. The splitting (bifurcation) of mushroom diameter distribution on the large and small mushroom spikes increases with radial distance from the center of Gaussian-like spot. Dynamics of their evolution is represented by the orbits or stable periods in 2D phase space. The constant mushroom diameter – stable circulation or the stable periodic orbits – are the *limit cycles* between the unstable spiral orbits. Those with increasing periods represent supercritical Hopf bifurcation, while those leading to decrease and disappearance represent subcritical Hopf bifurcation. The *empirical models* of RMI, although predict dependence of the growth rate on radial distance (distance the reshocks travel to reach the interface), show many limitations. More appropriate interpretation of the simultaneous growth and lattice organization of small and large spikes give the *fundamental model* based on the interference of the perturbation modes depending on their amplitude, relative phase, and the symmetry. The late-time instability in the base-plane evolves into line solitons, vortex filaments and wave–vortex structures with chaotic rather than stochastic features.

Keywords: Hopf bifurcation; Laser ablation; Lattice of mushroom spikes; Rayleigh–Taylor instability; Richtnyer–Meshkov instability; Small and large mushroom spikes; Solitary waves; Wave–vortex phenomena

1. INTRODUCTION

The Richtmyer–Meshkov instability (RMI) (Richtmyer, 1960; Meshkov, 1969) occurs for the impulsive acceleration of either the light fluid into the heavy one, or vice versa. Growth of spikes and bubbles and subsequent mixing arise when a shock passes through an interface between two fluids (Wouchuk & Nishihara, 1996; Zabusky, 1999). The light fluid (ρ_L) is accelerated impulsively into the heavy one (ρ_H) causing baroclinic vorticity deposition. In the presence of the re-shock, additional vorticity is deposited during its interaction with the evolving interface (Yang *et al.*, 1990; Brouilette & Sturtevant, 1994; Balakumar *et al.*, 2008; Probyn & Thornber, 2013). Lugomer, 2016. With the passage of a shock front, the interface begins to decelerate after shock refraction. Since the pressure decreases monotonically with distance behind the shock front, the reversal of pressure and of density gradients occurs from the heavy into the light fluid. Such a condition at the interface causes the Rayleigh–Taylor instability (RTI) (Miles *et al.*, 2005). Under the influence of the RMI/RTI, interface perturbations grow into spikes of heavy-fluid into light-fluid and bubbles of light-fluid into heavy-fluid. Development of shear along the growing spikes causes the Kelvin–Helmholtz (KH) instability and formation of mushroom-shape spikes (Miles *et al.*, 2005; Lugomer, 2017).

The evolution of three-dimensional (3D) RMI and RTI on metal surface induced by the laser beam of Gaussian-like power profile in the semiconfined configuration (SCC) is

*Address correspondence and reprint requests to: S. Lugomer, Rudjer Boskovic Institute, Center of Excellence for Advanced Materials and Sensing Devices, Bijenicka c. 54, 10000 Zagreb, Croatia. E-mail: lugomer@irb.hr

of special interest and reveals some new characteristics (Lugomer, 2016, 2017). The nanosecond laser pulse causes plasma detonation and the shock wave that strikes the interface of the vapor/plasma plume [light fluid (ρ_L)] and the molten metal layer [heavy fluid (ρ_H)], with baroclinic vorticity deposition and the RMI evolution. The initial multimodal perturbation of the interface determines the amplitude and the wavelength of growing spikes and bubbles. The anisotropic flow and growth of spikes and bubbles depends on the *momentum*, $\boldsymbol{M}$, transferred to the fluid parcel and on the fluid density ratio expressed by the Atwood number, $A = (\rho_H - \rho_L)/(\rho_H + \rho_L)$ (Lugomer, 2016, 2017). Due to Gaussian power profile the A number laterally decreases from the central region (CR) to the near central region (NCR) and to the near periphery region (NPR) coinciding with decrease of the momentum transfer $\boldsymbol{M}$ to the density interface, and reveals many new RMI/RTI characteristics, which offer a new insight into these phenomena. Previous studies have shown the evolution of the new wave–vortex paradigm in the CR and NCR of Gaussian-like spot (Lugomer, 2016, 2017).

The RMI morphology in the CR resembles the irregular "egg-carton" web with cavities of collapsed bubbles surrounded by irregular "walls" formed at $A \sim 1$–0.85, $\boldsymbol{M} \sim \boldsymbol{M}_{max}$ (Lugomer, 2016). Formed as the crests of a heavy fluid around the bubbles, the "walls" are developed during non-linear growth when the instability amplitude becomes comparable with the perturbation wavelength λ (Srebro *et al.*, 2003; Reckinger, 2006). The connected walls form irregular web in a random flow field, while in the coherent one form a quasi-periodic polygonal or the rosette-like web. The RMI jet-spikes formed at the nodal points of a web are broken up into nanodroplets similar to that observed in the simulation (Statsenko *et al.*, 2006, 2014). Thus, dominant characteristic is – the absence of the mushroom shape spikes – and presence of their remnants slightly higher than the rest of the surface.

The morphology in the NCR formed at $A \sim 0.85$–0.65, $\boldsymbol{M} \sim (0.70$–$0.60)$. $\boldsymbol{M}_{max}$ is different from the CR (Lugomer, 2017) because the RMI is followed by the reversal of pressure and density gradients with onset of the RTI (Miles *et al.*, 2005; Suponitsky *et al.*, 2013, 2014).The interface perturbations grow into spikes of heavy-fluid into light-fluid and bubbles of light-fluid into heavy-fluid. The density interface of NCR is transformed into the large-scale irregular quasi-periodic web – which in contrast to the CR – comprises the large mushroom-shape spikes. Dynamics in the vertical direction differs dramatically from that in the horizontal (normal) plane, and can be regular (periodic) or quasi-periodic, or disordered (Abarzhi & Hermann, 2003; Abarzhi, 2008; Abarzhi, private communication).

In this paper, we consider the NPR morphology of RMI/RTI structures formed at $A \sim 0.60 < 0.2$, $\boldsymbol{M} \sim (0.50 \leq 0.2)$. $\boldsymbol{M}_{max}$ evolves due to the shock and fast reshocks. Morphology evolves into quasi-periodic web with cavities surrounded by irregular "walls"– and with large and small spherical mushroom-shape spikes on disordered two-dimensional (2D) lattice. Disorder is associated with the reshocks, which become oblique and randomly oriented increasing the inhomogeneity of the fluid flow field with deformation of the web structure. In such environment, the organization of mushroom spikes on 2D lattice is different in the domains at various distances from the center of the spot. Intuitively, the new characteristics like dependence of diameter of large and small mushroom spikes with radial distance, as well as dependence of the growth rate on the interface shape (i.e., on the large and small wavelength modes) can be expected. Since the surface corrugations are inhomogeneous, the perturbation modes may be assumed grouped into narrow bands of short and large wavelength modes with different effect on the growth rate.

The basic question is, whether characteristics of RMI/RTI morphology like for example, the growth rates and formation of large and small mushroom spikes, can be explained by a model that would be able to predict the formation of both, the small and the large mushroom spikes on 2D lattice and, and their simultaneous evolution in the subdomains at various distance from the center of the spot. Therefore, the comparison of the experimental results with prediction of *empirical multiparameter models* and also with prediction of the more *fundamental model based on the first principles*, will be performed.

The *empirical models* of the RMI based on the evolution of the multimodal perturbation occurring after the shock and reshocks (Mikelian, 1989; Leinov *et al.*, 2009; Ukai *et al.*, 2011), indicate the spike growth rate dependence on the distance the reshock travels in order to reach the interface, and on the interface shape at the moment of its arrival. Levinov *et al*., have shown that reshock arrival to the interface during the linear growth (before the arrival of the reflected rarefaction wave), will cause the fast linear growth. The reshock arrival during slower, non-linear growth (before the arrival of the reflected rarefaction wave), will progressively decay and the spikes will be small (Leinov *et al.*, 2009). As shown latter, these models although explain some of the observed phenomena depend on adjustable parameters and suffer from many shortcomings.

The model of the RMI evolution from the *first principles* with interference of initial perturbation modes (without reshock) was recently proposed by Abarzhi and co-workers (Pandian *et al.*, 2017; Stellingwerf *et al.*, 2016*a*, *b*). Based on the group theory analysis and the smooth particle hydrodynamics (SPH) simulation their model shows simultaneous evolution of large and small mushroom-shape RMI spikes on 1D lattice resulting from interference of initial perturbation modes. In contrast to usual studies based only on the amplitude of perturbation modes, their model takes into account the amplitude, relative phase, and the symmetry of the wave vectors on the reciprocal lattice, with various A number values (Pandian *et al.*, 2017; Stellingwerf *et al.*, 2016*a*, *b*). The results obtained by superposition of perturbation waves on 1D lattices with random phase, in-phase, and

https://doi.org/10.1017/S0263034617000611 Published online by Cambridge University Press

anti-phase offer more promising (successful) comparison with the experimental ones.

Discussion of the non-linear phase of the RMI evolution with the large-scale coherent structures chaotically arranged as the "late time structures" and the absence of the stochastic small-scale turbulence mixing (Lugomer, 2016, 2017), is presented.

The paper is organized as follows: INTRODUCTION; OUTLINES OF THE EXPERIMENT – Expansion of metal vapor–plasma spheroid along the SCC microchannel in the ambient gas; RESULTS AND DISCUSSION – Quasi-periodic, chaotic, or broken web; Spherical mushroom spikes; ORGANIZATION OF MUSHROOM SPIKES – Lattice organization of large and small mushroom spikes; Off-lattice random organization of very-large and very-small mushroom spikes; Characteristics of mushroom diameter distribution across the NPR; Representation of mushroom diameter by orbit in phase space; GROWTH RATE OF SMALL AND LARGE MUSHROOM SPIKES – Dependence of the growth rate on the distance the reshock has to travel; Dependence of the growth rate on the interface shape; Multiscale mushroom spike evolution caused by the interference of perturbation modes: Non-linear dynamics of RM flow; Characteristics of the low-mixing structures in the base-plane; and CONCLUSION.

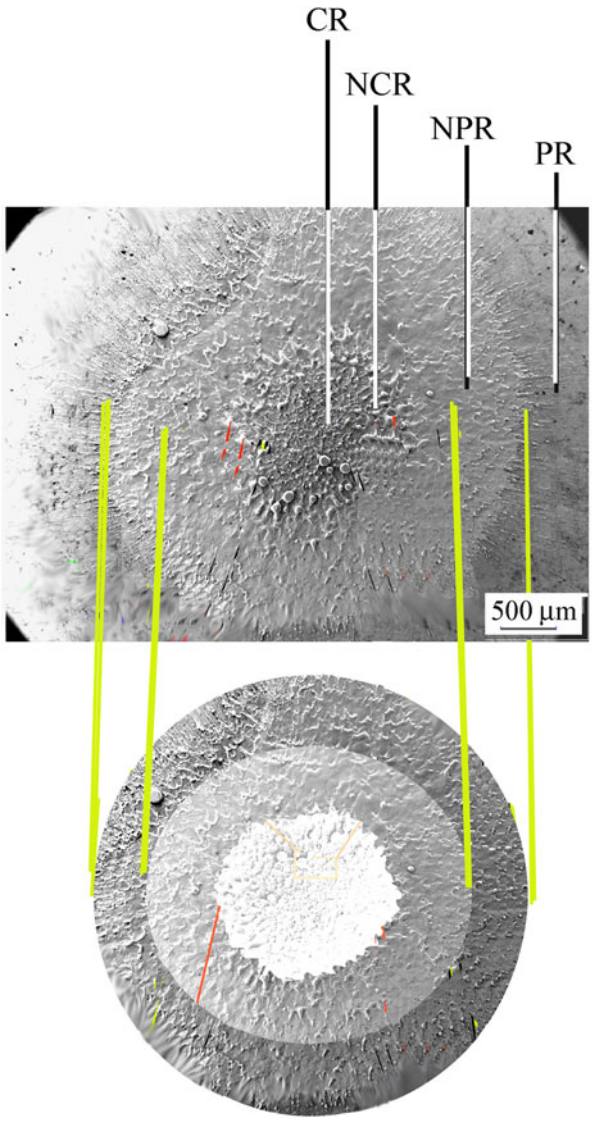

Fig. 1. SEM micrograph of the spot on indium surface after irradiation by Gaussian-like pulse of a ruby laser in the SCC with excerpt of the central region (CR), near central region (NCR), and the near periphery region (NPR). The NPR morphology (outer ring) is better seen in the magnified excerpt from the spot.

2. OUTLINES OF THE EXPERIMENT

The experiments were performed in the SCC in which the target is irradiated through transparent quartz plate positioned at $\Delta \sim 120$ μm above the target surface (Lugomer, 2016, 2017). Irradiation was performed by a single pulse of a Q-switched ruby laser $E \sim 160$ mJ ($E_s \sim 12$ J/cm^2; $P_s \sim 0.48 \times 10^9$ W/cm^2 (~0.5 GW/cm^2); $\tau = 25$ ns, $\lambda =$ 628–693 nm). Indium plates of 1 cm × 1 cm × 0.1 cm, as a soft material with the melting point $T_M = 429$ K and boiling point $T_B = 2345$ K, were used as targets. Schematic representation of the experiment is given in the papers I and II (Lugomer, 2016, 2017). The sample was situated in the gas chamber and irradiated in the presence of air as a background gas at the pressure $P_0 = 1$ atm, and the area irradiated was $S = 0.013$ cm^2. The target surface was prepared by making small and the large-scale random corrugations (scratches) with the scratch–scratch distance, $d_{\text{large scratch}} \sim 10$–60 μm and the amplitude $a_0 \sim 10$–20 μm. Multimodal perturbation of density interface consisted of a random combination of incomensurate short- and long-wavelength modes.

Absorption of laser energy causes plasma ignition and detonation with generation of a shock wave in the SCC microchannel. The shock wave traveling downward strikes the ρ_L/ρ_H interface causing deposition of baroclinic vorticity (Fig. 1a–d and description in the Supplement of the paper I). The shock wave traveling upward is reflected from the cover plate. The reflected shock wave as (from the cover plate or the target surface), as well as the lateral plume expansion in the ambient gas is called reshock [Figs 1e–h of the paper I (Lugomer, 2016)].

2.1. Expansion of Vapor–Plasma Spheroid along the SCC Microchannel in the Ambient Gas

Radial plasma expansion causes the compression of surrounding background gas (air) and formation of the air shell (Ma *et al.*, 2010). Compression increases the ion number density in the radial direction causing minimum in the center of its distribution. The initial density which becomes very low in the CR, increases to the NCR and continues to increase to the NPR, $\rho_L(\text{CR}) < \rho_L(\text{NCR}) < \rho_L(\text{NPR})$. Since the density of a heavy fluid is the same in all regions $\rho_H(\text{CR}) = \rho_H(\text{NCR}) = \rho_H(\text{NPR})$, the Atwood number

https://doi.org/10.1017/S0263034617000611 Published online by Cambridge University Press

decreases across the spot below the Gaussian power profile in the radial direction from $A(\mathrm{CR}) > A(\mathrm{NCR}) > A(\mathrm{NPR})$.

The evolution of mushroom spikes and the base-plane structures forms the morphology, which stays frozen permanently by the fast solidification after termination of interaction making possible *a posteriori* study by the scanning electron microscope (SEM) JEOL.

3. RESULTS AND DISCUSSION

3.1. Quasi-Periodic, Chaotic, or Broken Web

Gaussian-like spot with the excerpt of the CR, the NCR, and the NPR is shown in Figure 2. Morphological structure reveals broken "egg-cartoon" web with cavities – formed by one or more bubbles – surrounded by irregular "walls". Figure 2. The "walls" are the crests of a heavy fluid around the bubbles, or around a bubble cluster, or the – "curtains between the bubbles" – developed during non-linear growth when the instability amplitude is of the order of λ (Reckinger, 2006). The "walls" connected into the *quasi-periodic web* comprise deformed cells (bubble/cavities) with the "wavelength", λ from ~40 to ~60 μm, which may be attributed to the long-wavelength surface perturbation by corrugation, $d_{\mathrm{scratch}} \sim 40$–$60$ μm (Lugomer, 2016). Such structures may be attributed to the characteristic momentum transfer, $\boldsymbol{M}$, which decreases across the NPR ($0.6\ \boldsymbol{M}_{\max} \gtrsim \boldsymbol{M} \lesssim 0.2\ \boldsymbol{M}_{\max}$), and to the decrease of the A number ($0.60\ A \gtrsim 0.2$) due to lateral vapor expansion along the SCC microchannel, which causes increase of the density of the low-density fluid ρ_{L} (Lugomer, 2016).

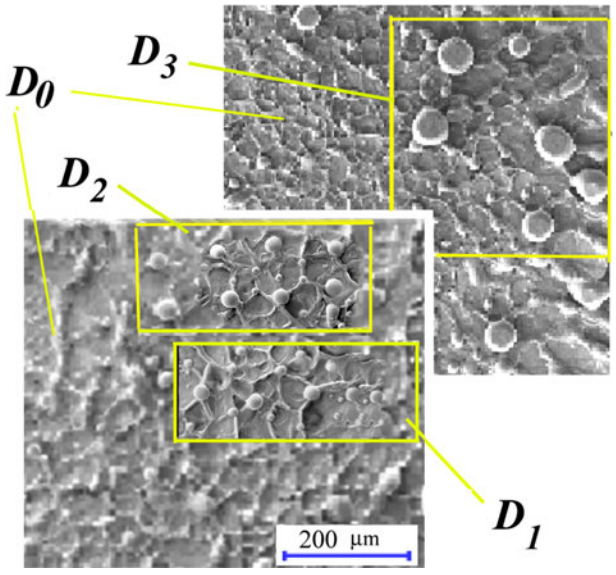

Fig. 2. SEM micrograph of RMI/RTI morphology typical for NPR. Dominant structure is irregular polygonal web which does not show mushroom shape spikes at the nodal points (domain $\boldsymbol{D}_0$). SEM analysis reveals inside $\boldsymbol{D}_0$ the subdomains $\boldsymbol{D}_1$ and $\boldsymbol{D}_2$ (at the same distance from the center of the spot), which comprise many small and large spherical mushroom spikes on disordered 2D lattice, as well as the subdomain $\boldsymbol{D}_3$ with off-lattice very-large mushroom spikes.

Quasi-periodic web may be compared with 3D numerically simulated large-scale periodic RMI structures generated by both, the single-mode (Miles *et al.*, 2005; Long *et al.*, 2009) and the multimode perturbations (Cohen *et al.*, 2002; Kartoon *et al.*, 2003). A large periodic structure (for the shock tube experiment) is obtained for the vertical interface oscillation in a square cell due to the single-mode 3D perturbation

$$z(x, y) = a_0 \cos(k_x x) \cos(k_y y), \tag{1}$$

where $a_0 = 3.45$ mm, $k_x = k_y = \sqrt{2}\,\pi/W$, and $W =$ width of the test section, for the weak shock of $Ma = 1.22$, and the low Atwood number $A = 0.65$ (Long *et al.*, 2009).

Transformation of regular periodic web into deformed, quasi-periodic or chaotic, or even into broken one is caused by the bubble shape oscillations driven by the fast oscillatory reshocks ($\nu \sim 7$–8 MHz), and to the effect of the reshocks on the fluid shear layer (Lugomer, 2016). High-frequency field of re-shocks generates the pressure gradient, which couples with the bubble oscillations (volume pulsations) and vorticity generation in the ultrasonic field (Leighton *et al.*, 1990). When the reshock strikes the density interface as rarefaction wave, the molten indium is subjected to tension, which causes it to cavitate (Suponitsky *et al.*, 2013; Lugomer, 2016). Pressure pulsations take place in the mixing zone owing the vortex character of mixing and the pressure field, which is irregular in vortices (Suponitsky *et al.*, 2013). Irregularity of the pressure field causes distortion of the shock wave front and of the RMI surface morphology. Forcing of the oscillating pressure field on the bubbles of different size causes bubble dynamics, which generates waves with irregular front in the surrounding fluid. The waves solidified in the fast cooling process make the irregular "walls" of variable shape and size (around the bubbles). Connected into quasi-periodic or even chaotic web of broken "egg-cartoon" morphology, they are characteristic for random (incoherent) flow field (Lugomer, 2016).

RMI mushroom spikes do not appear at the nodal points of a web, but mostly hillock-like humps with the exception of some (random) nodal points. Large incoherent flow field does not show evolution of coherent flow domains with polygonal or the rosette-like web as in the CR and NCR (Lugomer, 2016, 2017). SEM analysis reveals that such large irregular and chaotic or broken web without mushroom spikes (denoted domain $\boldsymbol{D}_0$) – comprises few subdomains ($\boldsymbol{D}_1$, $\boldsymbol{D}_2$, and $\boldsymbol{D}_3$) with large and small RMI mushroom spikes. Figure 2. For the obvious reasons we shall not consider domain $\boldsymbol{D}_0$ but only subdomains $\boldsymbol{D}_1, \boldsymbol{D}_2$, and $\boldsymbol{D}_3$, which comprise the spherical mushroom spikes organized on disordered 2D lattice.

3.2. Spherical Shape of Mushroom Spikes

Formed at the nodal points of a web the spherical RMI mushroom spikes are similar to that in the NCR (Lugomer, 2017),

https://doi.org/10.1017/S0263034617000611 Published online by Cambridge University Press

and to that obtained by 3D numerical simulation for the single-mode perturbation (Anuchina *et al.*, 2004). Similarity with spherical spikes generated by the single-mode perturbation indicates that in the multimodal perturbation not all modes are equally active; only a narrow band of modes (concentrated around one central wavelength mode) acts as the single-mode perturbation. Absence of the elongated prolate, or damped spikes (lack of the shape variation of the mushroom spikes) relates to the specific values of the A number, but also of the Eötvös number, Eo, and the Morton number Mo (Lugomer, 2017). Bubble can be characterized by the Morton number $Mo = g\mu_l^4/\rho_l\sigma^3$, by the Eötvös number, $Eo = \rho_l g d_l^2/\sigma$, as well as by density (ρ_l/ρ_b) and viscosity (μ_l/μ_b) ratios, where d_l is the effective radius of the bubble, index, l, relates to liquid and, b, to the bubble (gas) (Unverdi and Trygvason, 1992). Morton number involves the fluid properties only, and the Eötvös number is the non-dimensional size of the bubble. The analysis of the mushroom shapes (Lugomer, 2017), indicates that the spherical shape in $\boldsymbol{D}_1$. $\boldsymbol{D}_2$, and $\boldsymbol{D}_3$ may be characterized by $Eo \gtrsim 10^2$ and $Mo \sim 10^2$.

4. ORGANIZATION OF THE MUSHROOM SPIKES

Expansion of laterally accelerated shear layer with the velocity $u \sim 1650$ m/s (the sonic velocity in liquid indium), is associated with variation of thickness and velocity due to reshocks (Lugomer, 2017). The reshocks become oblique and randomly oriented (due to irregularity of the interface), increasing the inhomogeneity of the fluid flow field. This not only causes quasi-periodicity or chaos of the web structure, but also disturbs the organization of spikes in various subdomains of the NPR. The subdomains $\boldsymbol{D}_1$ and $\boldsymbol{D}_2$, show organization of spikes on disordered 2D lattices, while $\boldsymbol{D}_3$ shows very-large off-lattice mushroom spikes (Fig. 2).

4.1. Lattice Organization of Large and Small Mushroom Spikes

Regarding the mushroom spike organization in $\boldsymbol{D}_1$, the SEM micrograph shows irregular (chaotic) web of the base-plane structures and the large and small mushroom spikes with the particle number density of $\rho_N \sim 5 \times 10^4/\text{cm}^2$ (Fig. 3). Neglecting the base-plane structures, the mushroom spikes reveal 2D disturbed lattice organization. Reconstruction of regular lattice from Figure 3 starts with conformal mapping of small (blue) and large (red) mushroom spikes (Fig. 4a). The rows of spikes coincide with uncorrelated (chaotic) wavy instabilities in the molten layer (background fluid) (Fig. 4b). Incoherent wavy motion of background fluid is the consequence of fast reshocks, which after series of reflections change the strength and direction of the wavy motion. By continuous deformation the wavy rows of mushroom spikes can gradually be transformed into the rectangular lattice

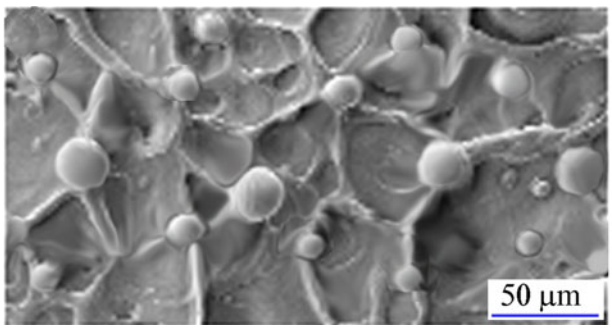

Fig. 3. SEM micrograph of subdomain $\boldsymbol{D}_1$ (with small rendering) showing large and small spherical mushroom spikes formed at the nodal points of irregular web.

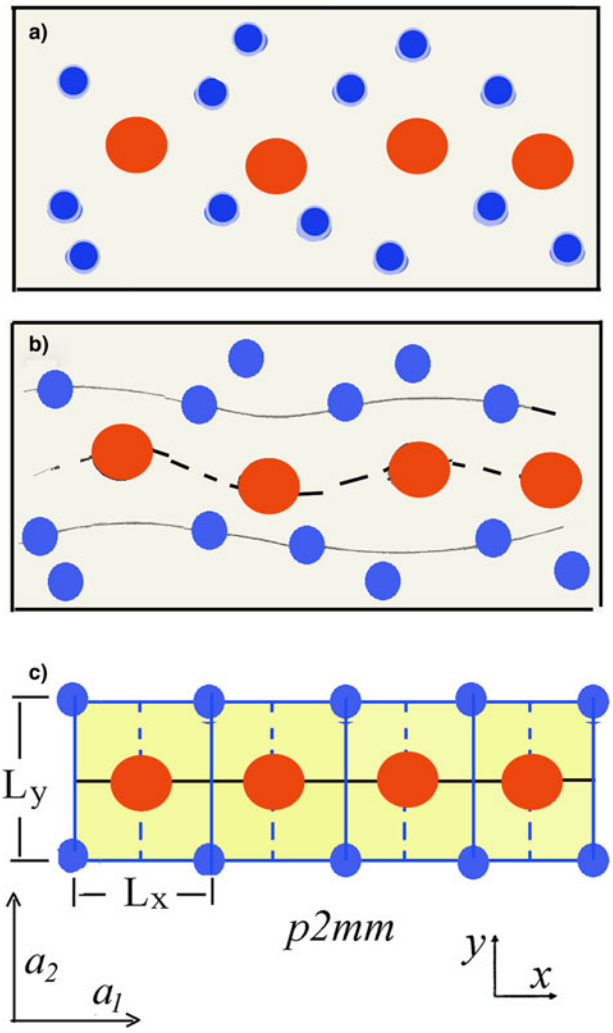

Fig. 4. Organization of small (blue) and large (red) mushroom spikes in the form of disordered lattice, and identification of the closest hypothetical 2D regular lattice to which the observed pattern might belong. (a) Map of the large and small mushroom spikes that corresponds to their organization in Figure 3. (b) Disordered organization of small and large mushroom spikes caused by the instability (wavy motion) of the surface molten layer. (c) Reconstruction of the mushroom spike organization on a 2D regular p_2mm lattice. The basic cell is the rectangular configuration of four small spikes and one large spike at the center of inversion.

https://doi.org/10.1017/S0263034617000611 Published online by Cambridge University Press

(Fig. 4c) with the primitive cell size of, $L_y \sim 80$–90 μm, and $L_x \sim 60$–70 μm. By extending this arrangement to the whole plane, a pattern is obtained that belongs to the p_2mm symmetry group with the translation vectors $\mathbf{a}_1$ and $\mathbf{a}_2$ (Fig. 4c), having lengths $a_1 = L_x \sim 60$–70 μm, $a_2 = L_y \sim 80$–90 μm. The repeating structural unit is made of one large and four adjacent small mushroom spikes. The diameter of the large mushroom spike is, $D_{LM} \sim 25$ μm and of the small one, $D_{SM} \lesssim 15$ μm.

SEM micrograph of $\mathbf{D}_2$ shows irregular (chaotic) web as the base-plane structure, and the large and small mushroom spikes on its nodal points with $\rho_N \sim 3 \times 10^4/\text{cm}^2$ (Fig. 5a). The RMI spherical mushroom spikes on 2D disordered lattice are organized in two rows of large- and two rows of small spikes between them (Fig. 5a). The small spike is connected with the two nearest large mushroom ones under an angle of ~120° (Fig. 5b). The conformal map of disordered small and large mushroom spikes in Figure 6a reveals wavy rows, which coincide with uncorrelated (chaotic) wavy instability in the molten layer, as in the case above (Fig. 6b). Correction of the wavy rows reveals the lattice of p_2mm symmetry group (Fig. 6c). The size of the rectangular (cell) $L_y \sim 110$ μm, $L_x \sim 80$ μm is equal to the translation vectors of the lattice $\boldsymbol{a}_1$ and $\boldsymbol{a}_2$, $L_x = a_1$, ($a_1 \sim 80$ μm), and $L_y = a_2$ ($a_2 \sim 110$ μm). The side of the rhombic cell is $l \geq 49$ μm. The diameter of the large mushroom spike is $D_{LM} \lesssim 40$ μm and of the small one $D_{SM} \sim 10$–15 μm.

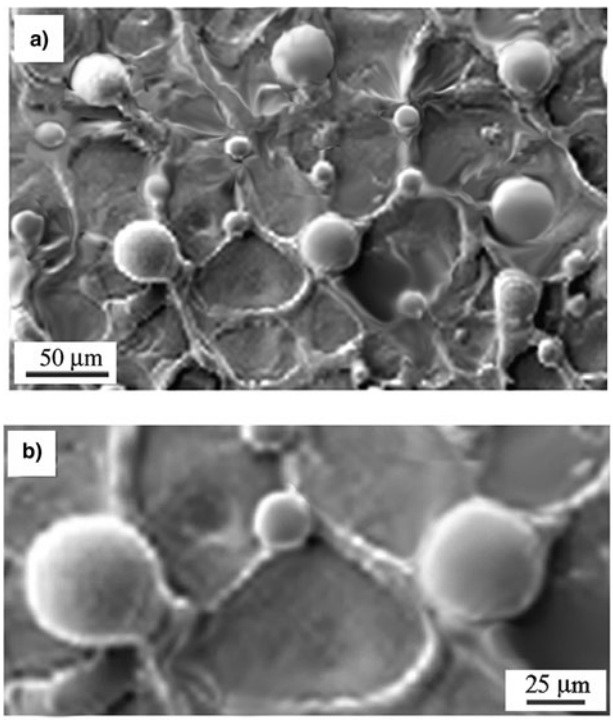

Fig. 5. SEM micrograph showing (with small rendering) RMI structures in subdomain $\boldsymbol{D}_2$. (a) Large and small spherical mushroom spikes formed at the nodal points of irregular web. (b) Enlarged segment from disordered lattice of spikes in Figure 5a.

4.2. Off-Lattice Random Organization of Very-Large and Very-Small Mushroom Spikes

SEM micrographs of subdomain $\mathbf{D}_3$ (Fig. 7a and b) also show irregular (chaotic) and partially broken web and very-large mushroom spikes with $\rho_N \sim 850/\text{cm}^2 \sim 9 \times 10^2/\text{cm}^2$ – about three orders of magnitude lower than the number

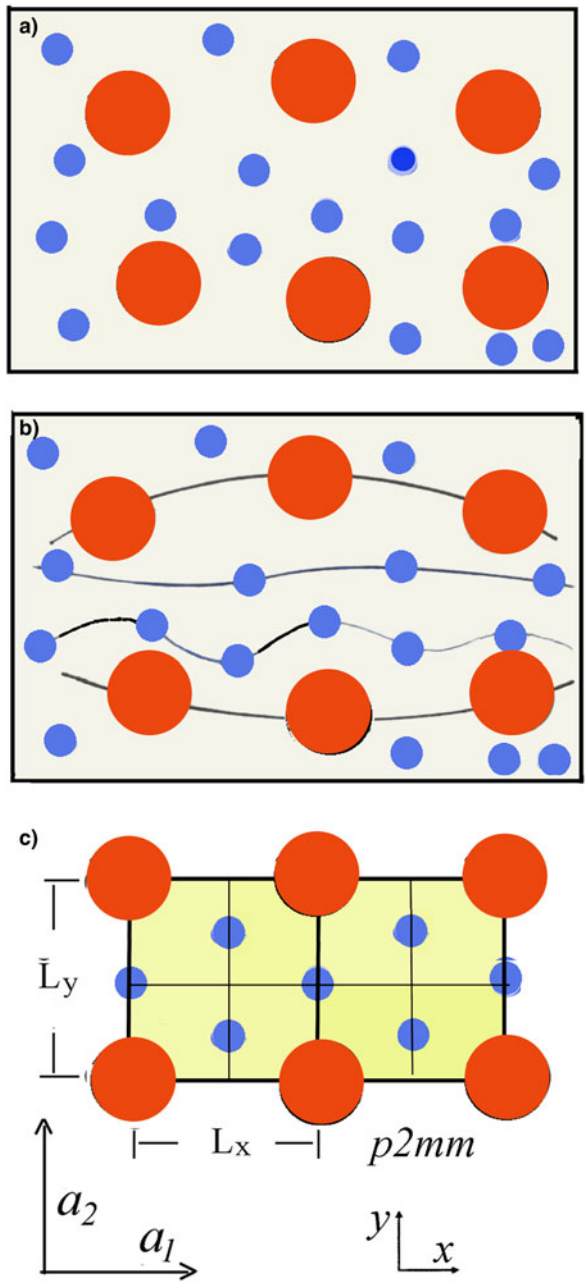

Fig. 6. Organization of small (blue) and large (red) mushroom spikes on disordered lattice, and identification of 2D regular lattice. (a) Map of the large and small mushroom spikes that corresponds to their organization in Figure 5. (b) Disordered organization of small and large mushroom spikes caused by the instability (wavy motion) of the surface molten layer. (c) Reconstruction of the mushroom spike organization on 2D regular lattice. The basic cell is the rectangular configuration of four large spikes and four small ones which make the rhombic subcell.

https://doi.org/10.1017/S0263034617000611 Published online by Cambridge University Press

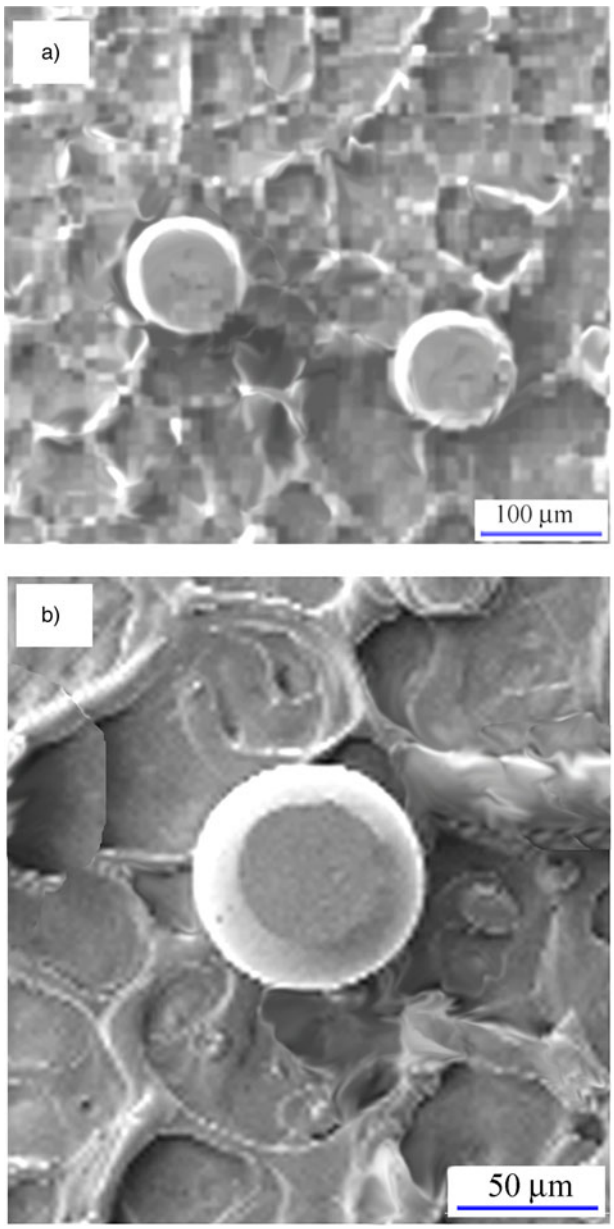

Fig. 7. SEM micrograph of RMI/RTI structures in subdomain $\boldsymbol{D}3$ showing irregular web structure in the base-plane and very-large spherical mushroom spikes. The top surface was flattened when the spherical mushroom spike reached the quartz cover plate that has stopped its growth. (a) SEM micrograph of two giant mushroom spikes with flattened top surface of diameter $D_{\mathrm{VLM}} \sim 80$ μm at the distance of $L \gtrsim 150$ μm. There are no small spikes in the vicinity, but only a small dots, which possibly are a very-small mushroom spikes. The base-plane structures of destroyed web are chaotically organized solitary waves and vortex filaments characteristic for the shallow fluid layer. (b) SEM micrograph of one very-large mushroom spike of diameter $D_{\mathrm{VLM}} \sim 70$ μm, of the height (amplitude) of, $h_{\mathrm{S}} \sim 120$ μm, which is just the height of the SCC channel. The growth rate of this spike is about 10–15 times faster than the growth rate of bubbles. The structures in the base-plane are disturbed and chaotically organized large-scale line-solitons or irregular ribbons, but transition to the small-scale turbulent structures does not appear.

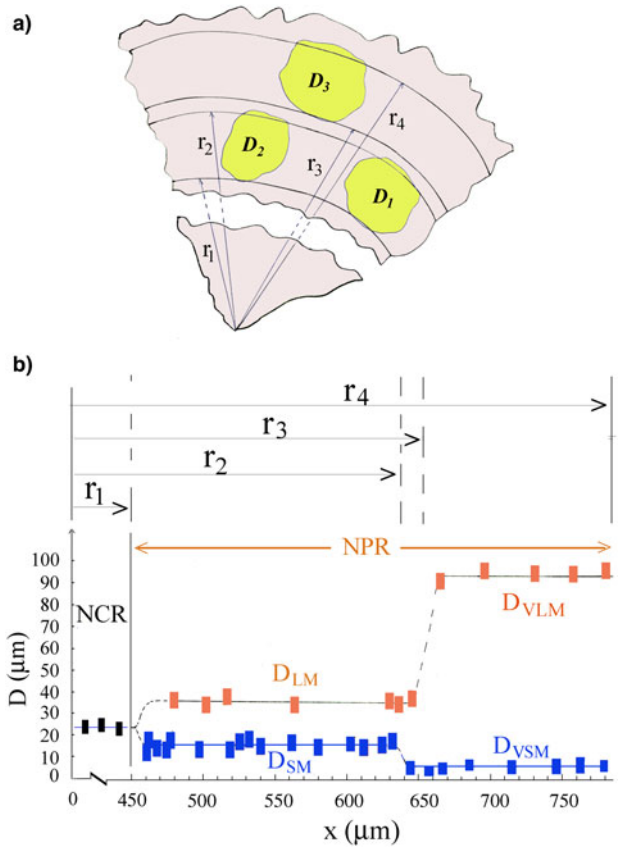

Fig. 8. Size distribution of mushroom spikes in various domains of the NPR. (a) Segment of the NPR corresponding to Figure 2, shows location of subdomains $\boldsymbol{D}_1$, $\boldsymbol{D}_2$, and $\boldsymbol{D}_3$. Domain $\boldsymbol{D}_0$ (which does not comprise mushroom spikes but only the irregular web) is not limited to some area segment of the NPR, but relates to the whole NPR between the radial distance r_1 and r_4. Subdomains $\boldsymbol{D}_1$ and $\boldsymbol{D}_2$ are in the same angular segment between the radial distance r_1 and r_2, while $\boldsymbol{D}_3$ is in more distant radial segment between r_3 and r_4. (b) Distribution diagram of the mushroom diameter D as function of radial distance, r, from the center of the spot (and the origin of the shock wave). Note that distribution in the NCR ($r < 450$ μm) shows unique mushroom diameter, of the average size, $\langle D \rangle \sim 25$ μm. However, between $r_1 \sim 460$ μm and $r_2 \sim 650$ μm (subdomains $\boldsymbol{D}_1$ and $\boldsymbol{D}_2$), the size distribution shows splitting into branch of the large mushroom diameter, $\langle D_{\mathrm{LM}} \rangle \sim 35$ μm, into branch of small mushroom diameter, $\langle D_{\mathrm{SM}} \rangle \sim 14$ μm, and into the third branch which continues from the NCR with $\langle D \rangle \sim 25$ μm. For the subdomain $\boldsymbol{D}_3$ between $r_3 \sim 650$ μm and $r_4 \sim 760$ μm, the size distribution shows strong divergence; the large spikes become very-large spikes $\langle D_{\mathrm{VLM}} \rangle \sim 90$ μm and the small ones become very-small mushroom spikes reaching average diameter $\langle D_{\mathrm{VSM}} \rangle \lesssim 4$ μm.

density of the spikes in Figures 3 and 5. These off-lattice spikes with the mushroom diameter, $D_{\mathrm{LM}} \sim 55$–100 μm, reach the height, $h_{\mathrm{S}} \sim 120$ μm, which is just equal to the distance of the cover plate from the target surface (Fig. 1 in the paper I, Lugomer 2016). The top surface is flattened because the spikes touched the cover plate of the SCC; otherwise they could reach the height of ~140 μm. Similarity of the spherical shape with the spikes in the NCR (Lugomer,

https://doi.org/10.1017/S0263034617000611 Published online by Cambridge University Press

2017) indicates the A number value of $A \leq 0.65$. The ratio of the spike and bubble amplitude, $h_s/h_b \sim 10$–15, which is possibly the highest ratio observed in the laser experiments.

The SEM analysis reveals no small spikes as in Figures 3 and 5, but only small random dots on the walls of the web; we assume them as very-small mushroom spikes. With the size between nano- and micro-scales they are one order of magnitude smaller than the small spikes in Figures 3 and 5. In some domains they can be hardly seen (Fig. 7a), while in other domains cannot be seen at all (Fig. 7b).

Regarding the bubble-cavities, two types can be seen: large flat bubble-cavities and the small curved ones. Since the curvature of the bubble depends on the density ratio and on the acceleration strength, the non-linear RMI bubbles are flattened for weak pressure fluctuations, and are curved for the strong pressure fluctuations (oscillations) of a series of fast reshocks in the SCC. Obviously, various local domains experience the reshocks-induced pressure variation strength (Bromwick & Abarzhi, 2016).

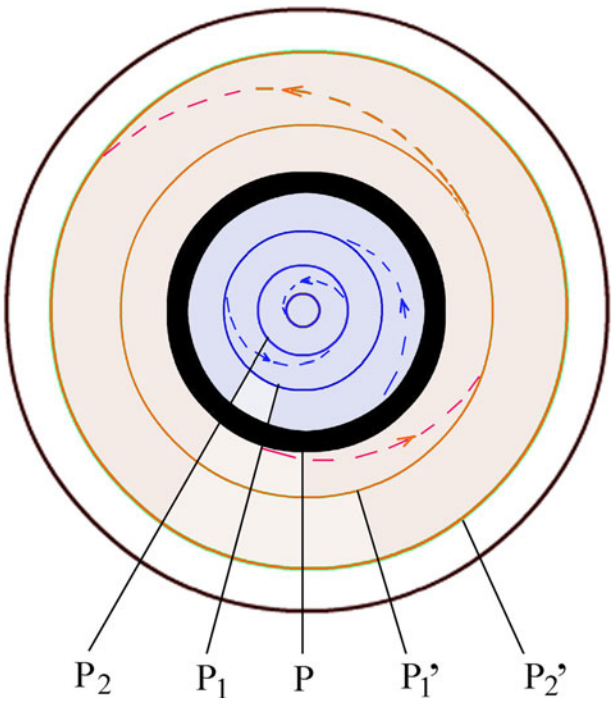

Fig. 9. Phase diagram of the "mixing and merging cycles" of spikes based on the diagram of the mushroom size distribution, D versus r, in Figure 8b. Mushroom spike diameter is represented by the orbit of certain radius or stable periods in 2D phase space. For the representation in phase space, we denote the constant mushroom diameter, $\langle D \rangle$, which continues from the NCR into NPR by the black periodic orbit P (stable circulation or constant oscillating frequency), which is the unique one for all mushroom spikes and not dependent on distance from the center. In the NPR, the small mushroom diameters $\langle D_{SM} \rangle$ and $\langle D_{VSM} \rangle$ are represented by the stable periods P_1 and P_2 (blue orbits) smaller than the period P. The large mushroom diameters $\langle D_{LM} \rangle$ and $\langle D_{VLM} \rangle$ are represented by the stable periods P_1' and P_2' (red orbits) larger than the period P. Note that P_1, P_2, P_1', and P_2' are the stable periods, while all other periods (between them) are unstable. Behavior of the unstable cycles resembles the kicked oscillator which is pushed from the stable oscillation into the unstable one until it falls into the stable period again. Thus, the periods represent the *limit cycles* of the Hopf bifurcation which depends on some dynamic parameter μ (see text). The unstable *red spiral orbits* change into larger and larger stable ones indicating supercritical Hopf bifurcation. The unstable *blue spiral orbits* change into smaller and smaller stable ones until finally vanish indicating subcritical Hopf bifurcation.

4.3. Characteristics of Mushroom Diameter Distribution across the NPR

The question is whether the size (diameter, D) of the large and small spikes in $\mathbf{D}_{1,2,3}$ have some correlation with the distance from the center the reshok(s) travels to reach the interface in particular subdomain as schematically shown in Figure 8a? Distribution of the mushroom spike diameter, $D(\mu m)$ as function of radial distance from the center, $r(\mu m)$, with distances of $\mathbf{D}_1$, $\mathbf{D}_2$, and $\mathbf{D}_3$ from the center of the spot are shown on the same radial axis (Fig. 8b). A monodispersed distribution of the mushroom diameters with the average size $\langle D \rangle \sim 25$ μm in the NCR extends up to $r \sim 450$ μm, but at $r \sim 460$ μm NPR becomes spitted into a band of small-diameter spikes, D_{SM}, into a band of large-diameter ones, D_{LM}, while the third branch with mushroom diameters $\langle D \rangle \sim 25$ μm, similar to that in the NCR continues from the NCR into NPR (Fig. 8b). Average diameter $\langle D \rangle \sim 25$ μm in both subdomains $\mathbf{D}_1$ and $\mathbf{D}_2$ intermittently increases (jumps) to $\langle D_{LM} \rangle \sim 35$ μm (large diameter ones), while other branch intermittently decreases (jumps) to $\langle D_{SM} \rangle \sim 14$ μm. Beyond $r > 650$ μm (subdomain $\mathbf{D}_3$), a new dramatic change occurs: the large spikes with $\langle D_{LM} \rangle \sim 35$ μm intermittently increase to the very-large mushroom spikes $\langle D_{VLM} \rangle \sim 90$ μm; the small ones with $\langle D_{SM} \rangle \sim 14$ μm, intermittently decrease to the very-small mushroom spikes with $\langle D_{VSM} \rangle \lesssim 4$ μm. For $r > 770$ μm (at the border of the PR), the RMI mushroom spikes vanish.

4.4. Representation of Mushroom Diameter by Orbit in Phase Space

More detailed insight into the dynamical evolution of small and large spikes can be obtained if the mushroom diameters are represented by orbits or stable periods. Namely, the vortex structure and fluid circulation on the spike, which form the mushroom shape (Anuchina *et al.*, 2004), correspond to the stable periods in the phase space. For the representation in 2D phase space, we denote the constant mushroom diameter in the NCR by the black circular orbit (stable circulation or constant oscillating frequency), which is the unique one for all mushroom spikes and not dependent on distance from the center (Fig. 9). In the NPR, the appearance of stable periodic orbits (the *limit cycles*) or their disappearance in a dynamical system indicates the Hopf bifurcation, described by the system of equations (Craford, 1991; Bressan, 2014)

$$dx/dt = mx + y + x^3, \tag{2}$$

https://doi.org/10.1017/S0263034617000611 Published online by Cambridge University Press

$$dy/dt = -x + my + y^3.$$

For $\mu < 0$, the origin is a stable point, and yields of an unstable periodic orbit; bifurcation is subcritical. For $\mu > 0$ the origin is unstable spiral and yields of a stable periodic orbit(s): bifurcation is supercritical (Bressan, 2014). Tentatively, the parameter μ can be defined as difference of the growth rates in the NPR, $dh/dt_{(NPR)}$ and in the NCR, $dh/dt_{(NCR)}$, $\mu = dh/dt_{(NPR)} - dh/dt_{(NCR)}$. Considering the phase portrait of dynamics in Figure 9, the red circles (orbits) at the outer side of the black one correspond to increase of the mushroom diameter with distance and tendency to stable orbits, indicating the *supercritical Hopf bifurcation* (Bressan, 2014), with $\mu > 0$. The blue circles (orbits) at the inner side of the black orbit indicate decrease of the mushroom diameter with distance and tendency to the point in the center (with disappearance of orbits), indicating the *subcritical Hopf bifurcation* with $\mu < 0$ (Fig. 9). Thus, simultaneous growth of large and small spikes – analogous to the rapid and slow growth rates – which shows divergence with distance may be represented by the supercritical and subcritical Hopf bifurcations.

5. GROWTH RATE OF SMALL AND LARGE MUSHROOM SPIKES

The growth rates of small and large mushroom spikes and dependence on distance cannot be considered on the basis of single-parameter RMI models depending only on the initial amplitude a_0 (Alon *et al.*, 1996; Shvarts *et al.*, 2001), which we used for the analysis of the spike growth in the CR (Lugomer, 2016) and NCR (Lugomer, 2017). More complex multiparameter models which consider the problem from *the empirical point of view* (Mikelian, 1989; Leinov *et al.*, 2009; Ukai *et al.*, 2011) are more appropriate as the first approach. These empirical models assume dependence of the growth rate of multimodal RMI on the reshock, and in this respect on the distance the reshock travels to strike the interface, as well as on the interface shape in the moment it arrives.

5.1. Dependence of the Growth Rate on the Distance the Reshock Has to Travel

Strong divergence of spitted distribution of mushroom diameters with r (Fig. 8b) indicates that the distance of particular subdomain $\mathbf{D}_{i\,=\,1,2,3}$, affects the growth rate. In addition, the fact that some spikes grow at small growth rate and others at the high rate, indicates that initial random multimodal perturbation does not affect the growth of all spikes in the same way. Since random surface corrugations are inhomogeneous, the small and large perturbation modes are grouped into narrow band of modes; the band of short-wavelength modes between $\lambda \sim 10$–30 μm, and the band of the large wavelength ones between $\lambda \sim 40$–60 μm. The short-wavelength band is concentrated around the central mode of, $\lambda_{short} \sim 20$ μm and the large wavelength one around $\lambda_{large} \sim 50$ μm with the corresponding amplitude of, $a_{0short} \sim 10$ μm and $a_{0large} \sim 20$–25 μm. Since the distances of the subdomains from the center [and of the shock wave origin, $r(\mathbf{D}_1) = r(\mathbf{D}_2) < r(\mathbf{D}_3)$], the reshock(s) strike the subdomains $\mathbf{D}_1$ and $\mathbf{D}_2$ in the same time – before the subdomain $\boldsymbol{D}_3$.

Leinov *et al.*, have shown dependence of post reshock(s) growth rates on distance and the corresponding times the reshock needs to reach the interface (Leinov *et al.*, 2009). Neglecting the perturbation amplitude of the interface, the reshock strength was found to be a dominant parameter; the evolution of the interface after passage of the reshock is influenced dramatically (Leinov *et al.*, 2009). If the reshock strikes the interface during the linear growth before the arrival of the reflected rarefaction wave, the post-reshock growth will continue to be the fast liner growth. The linear growth rate which is the result of a bubble competition process leads to formation of large spikes (and bubbles). If the reshock strikes the interface during slower, non-linear growth before the arrival of the reflected rarefaction wave, the post-reshock growth will progressively decay (Leinov *et al.*, 2009), and the spikes will be small.

5.2. Dependence of the Growth Rate on the Interface Shape

Dependence of the growth rate on the interface shape is characterized by the initial amplitude a_0, by the amplitude of oscillation after the first shock, the velocity jump after reshock, and the wavelength of perturbation. Many models have been proposed, some with controversial conclusion. The interface shape changes after the first shock, meaning that the moment when the reshock strikes it determines the growth rate of the spike in the post-reshock time. Dependence of growth rate on the above parameters that characterize the interface shape is usually transformed into dependence on the mixing length at reshock h_r, and the wave vector $\mathbf{k}$ of the perturbation modes (Ukai *et al.*, 2011). Considering only the *reshock models for multimodal perturbation* such as the model of Mikelian, the growth rate is given by (Mikelian, 1989; Ukai *et al.*, 2011)

$$dh_2/dt = C\Delta V_2 A^+, \tag{3}$$

where dh_2/dt is the growth rate after reshock, ΔV_2 is the velocity jump caused by the reshock, A^+ is the post-reshock A number, and C is the growth rate constant empirically determined, actually the adjustable parameter (Mikelian, 1989; Ukai *et al.*, 2011). In the Mikelian's model the growth rate is dependent on the parameter C ($C \sim 0.28$) indicating that the reshock growth rate is only a weak function of h_r and k, or not function at all.

https://doi.org/10.1017/S0263034617000611 Published online by Cambridge University Press

However, the study of single- and multi-modal 3D instability with reshock(s) has shown that the *rapid and slow growth rates* of spikes strongly depend on the interface shape (Ukai *et al.*, 2011), with different initial amplitudes and wave numbers – what makes the conjecture with our case. The rapid post-reshock growth occurs for the small amplitudes a_0 and wave numbers $k_{\max}$, which correspond to the Mikelian's growth rate constant ($0.81 < C < 0.93$), close to the single mode RMI growth rate (because the interface shape at the moment of the reshock arrival is still sharp and well resolved) (Ukai *et al.*, 2011). The slow post-reshock growth is caused by random initial interface shape (larger a_0 and $k_{\max}$), for 3D case correspond to the constant ($0.31 < C < 0.42$). In that case, the interface shape at the moment of the reshock arrival is a mixed and not sharp, because the complex mixing of spikes and bubbles carry lateral motion that cease the growth of the mixing length in the longitudinal direction and enhances the mixing of species (Ukai *et al.*, 2011). The model assumption is that a_0 and $k_{\max}$ (in non-dimensional units) are the only parameters that determine whether the mixing layer growth rate is rapid or slow. To quantify the initial perturbation they defined the Randomness factor R (Ukai *et al.*, 2011)

$$R = a_0 k_{\max}/L_y, \tag{4}$$

where L_y as the domain size in the y-direction is used to normalize the parameter. Thus, when R is small, the growth rates are similar to the single-mode cases. Thus, rapid 3D growth happens when $R \leq 0.2$ (Ukai *et al.*, 2011).

Considering the large spikes with rapid growth in our case, one has $a_0 \gtrsim 10$ μm, the domain size is about $L_y \sim 400$ μm, and wavelength in the band of short-wavelength modes, $\lambda \sim$ 10–30 μm. For the estimation of randomness factor R, the non-dimensional parameter, $k_{\max\ (\mathrm{ND})}$, has to be found. Taking, $k_{\max(\mathrm{ND})} = 2\pi/\lambda_{\min(\mathrm{ND})}$, where $\lambda_{\min(\mathrm{ND})} = \lambda_{\min}(\mu\mathrm{m})/\langle\lambda(\mathrm{mm})\rangle$, with $\lambda_{\min}(\mu\mathrm{m}) \sim 10$ μm is the minimal wavelength in the band, and $\langle\lambda(\mathrm{mm})\rangle \sim 15.5$ μm, is the average wavelength of the short-wavelength band of modes, gives $k_{\max(\mathrm{ND})} \sim 10$. Based on these parameters, $R \sim 0.2$ indicating that short-wavelength perturbation modes satisfy the Ukai's condition for the rapid growth.

Regarding the small spikes with slow growth and taking the initial amplitude $a_0 \sim 20$ μm, the domain size of $L_y \sim$ 400 μm, and the wavelength in the band of the long-wavelength modes, $\lambda \sim$ 40–60 μm, with $\lambda_{\min}(\mu\mathrm{m}) \sim 40$ μm, and $\langle\lambda(\mu\mathrm{m}) \sim 50$ μm, one has $k_{\max(\mathrm{ND})} \sim 7.9$. With these parameters one finds, $R = 0.395$, the value which satisfies condition for the slow growth, and which is also in agreement with the slow growth rate constant ($0.31 < C < 0.42$).

The conjecture between these empirical models and our experimental results besides similarities reveals two important differences: (i) The empirical models with adjusting parameters although explain the growth rate of large and small spikes cannot explain their formation on 1D or 2D lattice. (ii) These models cannot describe simultaneous formation of large and small spikes in the same subdomain, but of the large ones in one subdomain, and the small ones in other subdomain – at various distances and with different interface shapes.

5.3. Multiscale Mushroom Spike Evolution Caused by the Interference of Perturbation Modes: Non-linear Dynamics of RM Flow

More appropriate model for description of simultaneous formation of large and small mushroom spikes on 1D lattices from multimodal perturbation is a *fundamental model* derived from the first principles. The model is based on the group theory analysis and SPH numerical simulations (Pandian *et al.*, 2017, Stellingwerf *et al.*, 2016*a*, *b*). The growth (rate) of RMI small and large mushroom spikes on regular lattice emerges from the first shock and from the interface shape, and not from the reshock(s). The RMI evolution depends on the wavelength and amplitude but also on the relative phase of the initial perturbation modes. The model assumes that 2D flow spatially extended in the y-direction, periodic in the x-direction and invariant on 1D space groups. The initial multimodal perturbation is expressed by terms of wave vectors each of which corresponds to the symmetry position in the reciprocal lattice of the p_1 and pm_1 groups with translation operators. By using the two-wave initial perturbation, the evolution characteristics of RMI dynamics have been studied by the variation of relative phase of the waves ϕ, of the ratio a_2/a_1 (a_2 and a_1 are the amplitudes of the interfering waves 1 and 2), and of the A number ($A = 0.6$, 0.8, and 0.9). From the group theory aspect the superposition of perturbation waves on p_1 and pm_1 lattices with random phase $\phi_n = any$, in the first case, and $\phi_n = 0, 2\pi$ (in-phase) or $\phi_n = \pm\pi$ (anti-phase) in the second case, have been studied (Pandian *et al.*, 2017; Stellingwerf *et al.*, 2016*a*, *b*). The results obtained for $A = 0.6$ and the small amplitude of the second wave show the evolution of KH instability and formation of mushroom spikes. For the waves in *anti-phase* ($\phi = \pi$), the ratio of amplitudes a_2/a_1 determines the evolution of RMI dynamics. For $a_2/a_1 = 0.01$ the effects are insignificant, but they start to play some role for 0.1, while for 1.0 the interface morphology changes dramatically, because in the non-linear phase small mushroom-shape *spikes start to grow among the large ones* (Pandian *et al.*, 2017; Stellingwerf *et al.*, 2016*a*, *b*). The relative phase and interference of waves determine the RMI dynamics that influence qualitatively and quantitatively the symmetry, morphology, and growth rate of the unstable interface (Pandian *et al.*, 2017; Stellingwerf *et al.*, 2016*a*, *b*).

Based on this model the formation of spherical mushroom spikes on 2D p_2mm lattice can be interpreted by the interference of perturbation modes, which are in anti-phase and have the ratio of amplitudes, $a_2/a_1 \lesssim 1$. Lattice disorder, as seen in Figures 3 and 5, can be attributed to the series of fast reshocks, which cause the wavy perturbation of the background fluid and of the lattice of mushroom spikes.

https://doi.org/10.1017/S0263034617000611 Published online by Cambridge University Press

Intuitively, these effects should depend on the distance the reshocks travel to reach particular subdomain and affect the post-reshock RMI structure evolution.

5.4. Characteristics of the Low-Mixing Structures in the Base-Plane

SEM micrographs in Figures 3, 5, and 7 show in the base-plane the irregular web of non-linear solitary waves, breaking waves and ribbons as well as vortex filaments, that is, the coherent structures similar to that observed in the NCR (Lugomer, 2017). Horizontal acceleration causes the formation of non-linear waves in a thin fluid layer (*shallow fluid layer*), as well as their roll up into vortex filaments (for the Rayleigh number larger than the critical one, $Re \gtrsim 10^3$). The stochastic small-scale RMI turbulent mixing structures reported by many respected authors (Zhang, 1998; Cohen *et al.*, 2002; Anuchina *et al.*, 2004; Miles *et al.*, 2005; Long *et al.*, 2009; Youngs, 2013), are absent. Instead, the chaotic or quasi-regular organization of the large-scale coherent structures characterizes the non-linear evolution in the NPR. This problem is connected with the noise and fluctuations in RM/RT mixing called the interfacial RM/RT "turbulent mixing" (Zhang, 1998; Dimotakis, 2000). However, turbulence (at least canonical turbulence) is an equivalent of a stochastic process, where the flow fluctuations are independent of the initial conditions, boundary conditions and external forcing (Abarzhi, private communication). For canonical turbulence to occur the conditions of isotropy, locality, homogeneity, and statistical steadiness should be fulfilled. It may be said that in the case observed the RT and RM mixing flows do not obey these conditions. In contrast to turbulence – a chaos, while also appears as 'irregular', – depends on the initial conditions. In fact, their sensitivity to the initial conditions suggests that RT and RM mixing are more "chaotic" rather than stochastic processes (Abarzhi, private communication).

6. CONCLUSION

The NPR of Gaussian-like spot shows different morphology from the CR and the NCR. Due to the lateral vapor expansion in the SCC microchannel the ablated vapor is transported into the NPR. The change of morphology follows the change of momentum transfer $\mathbf{M}$ and the Atwood number A which continuously decrease across the NPR from about $\mathbf{M} \lesssim 0.65$ $\mathbf{M}_{max}$ to ~0.2 $\mathbf{M}_{max}$ and $A \sim 0.6$ to ~0.2 or less. Under moderate A and $\mathbf{M}$ parameters, a vertical shock wave causes growth of large and small RMI/RTI mushroom spikes organized on 2D rectangular lattice of p_2mm symmetry.

Distribution of the mushroom spike diameter as function of radial distance from the center of Gaussian-like spot shows that the monodispersed distribution in the NCR at the border of the NPR splits into a band of small-diameter spikes, and into a band of large-diameter ones. Divergence of splitted diameter distribution indicates divergence of growth rates of the spikes with increasing distance from the center of the spot (and of the origin of the shock wave). Evolution of small and large mushroom spikes is considered in the picture of dynamic system in which the mushroom diameter is represented by the orbit or stable periods in 2D phase space. For the corresponding phase portrait, the constant mushroom diameter is represented by the circular orbit (stable circulation or constant oscillating frequency), between unstable spiral ones. The unstable spirals leading to the stable periodic orbits (the *limit cycles*) represent supercritical Hopf bifurcation; those lading to their disappearance represent the subcritical Hopf bifurcation.

The growth rate of small and large RMI mushroom spikes is considered in the view of empirical models, which assume that the growth rate in multimodal perturbation depends on the reshock, and not primarily on the first shock. Consequently, the growth rate of mushroom spikes in various subdomains indicates *dependence on the distance the reshock has to travel, and dependence on the interface shape at the moment of the reshock arrival in particular domain.* In spite of the agreement of the growth rates for a given surface roughness parameter predicted by the model and the experimental ones, it was shown that these models cannot describe: (i) formation of mushroom spikes on 2D lattice, and (ii) simultaneous evolution of small and large mushroom spikes at the same distance (but the large spikes at one distance and the mall ones at the other distance).

More complete picture of 2D lattices of small and large mushroom spikes by multimodal perturbation after first shock gives the model based on the interference of perturbation modes taking into account the amplitude, relative phase and the symmetry of the wave vectors of the initial perturbation modes. The model for 1D periodic flow and formation of large and small spikes is based on the group theory and the SPH numerical simulations by Abarzhi and collaborators. The model can also describe more complex 2D periodic fluid flow and formation small and large mushroom spikes like that on a regular p_2mm lattice, observed in this case.

Lattice disturbance from ideal regular one can be attributed to the series of fast reshocks which cause the wavy perturbation of the background fluid (and of the lattice of mushroom spikes). Intuitively, this effect depends on the distance the reshocks have to travel to reach particular subdomain and on the shape of interface at that moment of its arrival.

The base-plane structures are not small-scale turbulent mixing ones, but the chaotic large-scale low-mixing solitary waves and vortex filament structures

ACKNOWLEDGMENTS

This work has been supported by the Croatian Science Foundation under the project: IP-2014-09-7046. I would like to thank to Professor N.J. Zabusky, Department of Physics of Complex Systems, Weizmann Institute of Science, Rehovot, Israel, for his comments of the wave–vortex paradigm in turbulent mixing in the laser experiments. I would also like to thank to Professor S. I. Abarzhi,

https://doi.org/10.1017/S0263034617000611 Published online by Cambridge University Press

Carnegie Mellon University, USA, for the inspiring comments of the chaotic and stochastic aspects of the mixing structures.

REFERENCES

Abarzhi, S.I. (2008). Coherent structures and pattern formation in Rayleigh–Taylor turbulent mixing. *Phys. Scr.* **78**, 015401.

Abarzhi, S.I. & Hermann, M. (2003). New Type of the Interface Evolution in the RMI. Annual Res. Briefs 2003, Center for Turbulence Research, Defense Tech. Inform. Center. (173–183). http://www.dtic.mil/cgi-bin/GetTRDoc?AD=ADP014801

Alon, U., Ofer, D. & Shvarts, D. (1996). Scaling Laws of Nonlinear RT and RM Instabilities, Proc. 5th Int.Workshop on Compressible Turbulent Mixing, ed. R. Young, J. Glimm and B. Boston, World Scientific. http://www.damtp.cam.ac.uk/iwpctm9/proceedings/.../Alon_Ofer_Shvarts.pdf

Anuchina, N.N., Volkov, V.I., Gordeychuk, V.A., Es'kov, N.S., Ilyutina, O.S. & Kozyrev, O.M. (2004). Numerical simulation of R–T and R–M instability using MAH-3 code. *J. Comput. Appl. Math*. **168**, 11–20.

Balakumar, B.J., Orlicz, G.C., Tomkins, C.D. & Prestridge, K.P. (2008). Dependence of growth patterns and mixing width on initial conditions in Richtmyer–Meshkov unstable fluid layers. *Phys. Scr. T* **132**, 014013.

Bressan, A. (2014). Math 417 – Qualitative theory of ODEs. https://www.math.psu.edu/bressan/PSPDF/M417-review4.pdf

Bromwick, A.K. & Abarzhi, S.I. (2016). Richtmyer–Meshkov unstable dynamics influenced by pressure fluctuations. *Phys. Plasmas* **23**, 112702.

Brouilette, M. & Sturtevant, B. (1994). Experiments on the Richtmyer–Meshkov instability: Single-scale perturbations on continuum interface. *J. Fluid Mech*. **263**, 71–292.

Cohen, R.H., Dennevik, W.P., Dimits, A.M., Eliason, D.E., Mirin, A.A., Zhou, Y., Porter, D.H. & Woodward, P.R. (2002). Three-dimensional simulation of a RM instability with two-scale initial perturbation. *Phys. Fluids* **14**, 3692–3709.

Craford, J.D. (1991). Introduction to bifurcation theory. *Rev. Mod. Phys*. **63**, 991–1035.

Dimotakis, P.E. (2000). The mixing transition in turbulent flows. *J. Fluid Mech*. **409**, 69–98.

Kartoon, D., Oron, D., Arazi, I. & Shvartz, D. (2003). Three-dimensional Rayleigh-Taylor and Richrmyer–Meskhow instabilities at all density ratios. *Laser Part. Beams* **21**, 327–334.

Leighton, T.G., Walton, A.J. & Pickworth, M.J.W. (1990). Primary Bjerknes forces. *Eur. J. Phys*. **11**, 47–50.

Leinov, E., Malamud, G., Elbaz, Y., Levin, L.A., Ben-Dor, G., Shvarts, D. & Sadot, O. (2009). Experimental and numerical investigation of the RM instability under re-shock conditions. *J. Fluid Mech*. **626**, 449–475.

Long, C.C., Krivets, V.V., Greenough, J.A. & Jacobs, J.W. (2009). Shock tube 3D-experiments and numerical simulation of the single-mode, 3D RM instability. *Phys. Fluids* **21**, 114104.

Lugomer, S. (2016). Laser generated Richtmyer–Meshkov instability and nonlinear wave paradigm in turbulent mixing. I. Central region of Gaussian spot. *Laser Part. Beams* **34**, 687–704.

Lugomer, S. (2017). Laser generated Richtmyer–Meshkov instability and nonlinear wave paradigm in turbulent mixing. II. Near-central region of Gaussian spot. *Laser Part. Beams* **35**, 210–225.

Ma, Q.I., Motto-Ros, V., Boueri, M., Bai, X.S., Zheng, L.J., Zheng, H.P. & Yu, J. (2010). Temporal and spatial dynamics of laser-induced Al plasma in Ar background at atmospheric pressure: Interplay with the ambient gas. *Spectrocim. Acta B* **65**, 896–907.

Meshkov, E.E. (1969). Instability of the interface of two gases accelerated by a shock wave. *Fluid Dyn*. **4**, 101–104.

Mikelian, K.O. (1989). Turbulent mixing generated by RT and RM instabilities. *Physica D* **36**, 343–347.

Miles, A.R., Blue, B., Edwards, M.J., Greenough, J.A., Hansen, F., Robey, H., Drake, R.P., Kuranz, C. & Leibrandt, R. (2005). Transition to turbulence and effect of initial conditions on 3D compressible mixing in planar blast-wave-driven systems. *Phys. Plasmas* **12**, 056317.

Pandian, A., Stellingwerf, R.F. & Abarzhi, S.I. (2017). Effect of a relative phase of waves constituting the initial perturbation and the wave interference on the dynamics of strong-shock-driven Richtmyer-Meshkov flows. *Phys. Fluids* **2**, 073903.

Probyn, M. & Thornber, B. (2013). Reshock of self-similar multi-mode RMI at high Atwood number in heavy-light and light-heavy configurations. 14th European Turbulence Conf., Lyon, France. etc14.ens-lyon.fr/openconf//request.php?

Reckinger, S. (2006). Development and applications of important interfacial Instabilities Rayleigh-Taylor, Rchtmyer–Meskhov, and Kelvin–Helmholtz, sales.colorado.edu/reckinger/Pubs/a1_fluids.pdf

Richtmyer, R.D. (1960). Taylor instability in shock acceleration of compressible fluids. *Commun. Pure Appl. Math* **13**, 297–319.

Shvarts, D., Sadot, O., Oron, D., Kishony, R., Srebro, Y., Rikanati, A., Kartoon, D., Yedvab, Y., Elbaz, Y., Yosef-Hai, A., Alon, U., Levin, L.A., Sarid, E., Arazi, L. & Ben-Dor, G. (2001). Studies in the Evolution of Hydrodynamic Instabilities and their Role in Inertial Confinement Fusion, IAEA, IF/7. www-pub.iaea.org/mtcd/publications/pdf/csp_008c/html/node263.htm

Srebro, Y., Elbaz, Y., Sadot, O., Arazi, L. & Shvarts, D. (2003). A general buoyancy-drag model for the evolution of the Rayleigh–Taylor and Richtmyer–Meshkov instabilities. *Laser Part. Beams* **21**, 347–353.

Statsenko, V.P., Sin'kova, O.G. & Yanilkin, Y.V. (2006). Direct 3D numerical simulation of turbulent mixing in a buoyant jet (in Russian). *VANT Ser. MMFP* **1**, 39–49.

Statsenko, V.P., Yanilkin, Y., Sin'kova, O.G. & Toporova, O.O. (2014). Numerical modeling of development of regular local perturbations and turbulent mixing for the shock waves of various intenisties. (in Russian). *VANT ser. Math. Model. Phys. Process*. **1**, 3–17.

Stellingwerf, R., Pandian, A. & Abarzhi, S.I. (2016*a*). Wave interference in Richtmyer–Meshkov flows. 69th Annual Meeting of the APS Division of Fluid Dynamics, November 20–22, 2016; Portland, Oregon, Vol. 61, Number 20. http://meetings.aps.org/Meeting/DFD16/Session/R18.6

Stellingwerf, R., Pandian, A. & Abarzhi, S.I. (2016*b*). Wave interference in Richtmyer–Meshkov flows. 58th Annual Meeting of the APS Division of Fluid Dynamics, October 31–November 4, 2016; San Jose, California, Vol. 61, http://meetings.aps.org/Meeting/DPP16/Session/YP10.52

Suponitsky, V., Barsky, S. & Froese, A. (2014). On the collapse of a gas cavity by an imploding molten lead shell and Richtmyer–Meshkov instability. *Comput. Fluids* **89.20**, 1–19. Science Direct. Web. 17 May 2014

Suponitsky, V., Froese, A. & Barsky, S. (2013). A parametric study examining the effects of re-shock in RMI. *Soft Condens. Matter* **2013**, 1–43. Arxiv. Web. 17 May 2014.

Ukai, S., Balakrishnan, K. & Menon, S. (2011). Growth rate predictions of single- and multi-mode RM instability with reshock. *Shock Waves* **21**, 533–546.

Unverdi, S.O. & Trygvason, G. (1992). A front-tracking method for viscous, incmpressible multi-fluid flows. *J. Comput. Phys*. **100**, 25–37.

Wouchuk, J.G. & Nishihara, K. (1996). Linear growth at a shocked interface. *Phys. Plasmas* **3**, 3761–3776.

Yang, X., Zabusky, N.J. & Chern, I.L. (1990). Breakthrought via dipolar-vortx formation in shock-accelerated density-stratified layers. *Phys. Fluids* **A2**, 892–895.

Youngs, D.I. (2013). The density ratio dependence of self-similar Rayleigh–Taylor mixing. *Philos. Transact. R. Soc.* A **371**, 20120173.

Zabusky, N.J. (1999). Vortex paradigm for accelerated inhomogeneous flows: Visiometrics for the RT and RM environments. *Ann. Rev. Fluid Dyn*. **31**, 495–536.

Zhang, Q. (1998). Analytical solutions of Lazer-type approach to unstable interfacial fluid mixing. *Phys. Rev. Lett*. **81**, 3391–3394.

https://doi.org/10.1017/S0263034617000611 Published online by Cambridge University Press